

Iron from a submarine source impacts the productive layer of the Western Tropical South Pacific (WTSP)

Cécile Guieu, Sophie Bonnet, Anne Petrenko, Christophe E. Menkès, Valérie Chavagnac, Karine V. Desboeufs, Christophe Maes, Thierry Moutin

▶ **To cite this version:**

Cécile Guieu, Sophie Bonnet, Anne Petrenko, Christophe E. Menkès, Valérie Chavagnac, et al.. Iron from a submarine source impacts the productive layer of the Western Tropical South Pacific (WTSP). Scientific Reports, 2018, 8, pp.9075. 10.1038/s41598-018-27407-z . hal-01819414

HAL Id: hal-01819414
https://hal.science/hal-01819414

Submitted on 21 Mar 2019

HAL is a multi-disciplinary open access archive for the deposit and dissemination of scientific research documents, whether they are published or not. The documents may come from teaching and research institutions in France or abroad, or from public or private research centers.

L'archive ouverte pluridisciplinaire **HAL**, est destinée au dépôt et à la diffusion de documents scientifiques de niveau recherche, publiés ou non, émanant des établissements d'enseignement et de recherche français ou étrangers, des laboratoires publics ou privés.

SCIENTIFIC REPORTS

OPEN

Iron from a submarine source impacts the productive layer of the Western Tropical South Pacific (WTSP)

Received: 12 September 2017
Accepted: 18 May 2018
Published online: 13 June 2018

Cécile Guieu[1,2], Sophie Bonnet[3], Anne Petrenko[3], Christophe Menkes[4], Valérie Chavagnac[5], Karine Desboeufs[6], Christophe Maes[7] & Thierry Moutin[3]

In the Western Tropical South Pacific, patches of high chlorophyll concentrations linked to the occurrence of N_2-fixing organisms are found in the vicinity of volcanic islands. The survival of these organisms relies on a high bioavailable iron supply whose origin and fluxes remain unknown. Here, we measured high dissolved iron (DFe) concentrations (up to 66 nM) in the euphotic layer, extending zonally over 10 degrees longitude (174 E—175 W) at ~20°S latitude. DFe atmospheric fluxes were at the lower end of reported values of the remote ocean and could not explain the high DFe concentrations measured in the water column in the vicinity of Tonga. We argue that the high DFe concentrations may be sustained by a submarine source, also characterized by freshwater input and recorded as salinity anomalies by Argo float *in situ* measurements and atlas data. The observed negative salinity anomalies are reproduced by simulations from a general ocean circulation model. Submarine iron sources reaching the euphotic layer may impact nitrogen fixation across the whole region.

The Western Tropical South Pacific (WTSP) Ocean has recently been identified as a hotspot of N_2 fixation[1], the main external source of new fixed nitrogen (N) to the surface ocean, which controls primary productivity and carbon export[2,3]. N_2-fixing organisms (or diazotrophs) have high iron (Fe) quotas relative to non-diazotrophic phytoplankton[4,5] and the success of diazotrophs in this region has been assumed to be due to the alleviation of Fe limitation[1]. As a result, there is considerable interest in studying and characterizing Fe sources in the WTSP in order to confirm or rule out this hypothesis. In the WTSP, Fe could be supplied by runoff from islands in the vicinity of Melanesian archipelagos[6] or by atmospheric volcanic inputs as the WTSP includes the Tonga and Vanuatu volcanic arcs. However, these potential Fe sources have not been quantified to date, even though it has recently been shown that volcanic aerosols facilitate natural Fe ocean fertilization around Iceland and the Mariana back-arc[7,8]. Recent numerical computer modeling has shed light on the crucial role played by hydrothermal Fe sources in global biogeochemical budgets, as these submarine sources are a major controlling factor in the column inventory of Fe in ~25% of the ocean[9]. Despite the facts that the WTSP comprises the most active zone for submarine volcanic activity in the world ocean[10] and that it has been identified as a priority zone to distinguish the trace metal sources of submarine origin from other sources[11,12], our knowledge on Fe sources in the WTSP remains fragmentary as only a very few dissolved Fe (DFe) data are available within the Melanesian region[13].

Here, we quantify the different Fe external sources (atmospheric and submarine) across a 4000-km zonal transect at ~19°S latitude in the WTSP (OUTPACE cruise, http://dx.doi.org/10.17600/15000900, Fig. 1A). We show that a shallow submarine source impacts DFe concentrations up to the productive layer (~0–140 m), where

[1]Sorbonne Université, CNRS, Laboratoire d'Océanographie de Villefranche, LOV, F-06230, Villefranche-sur-mer, France. [2]The Center for Prototype Climate Modeling, New York University in Abu Dhabi, Abu Dhabi, UAE. [3]Aix Marseille Université, CNRS/Institut National des Sciences de l'Univers, Université de Toulon, Institut de Recherche pour le Développement, Observatoire des Sciences de l'Univers Pythéas, Mediterranean Institute of Oceanography (MIO), F-13288, Marseille, France. [4]LOCEAN, Sorbonne Université, IRD/CNRS/MNHN, IRD, BP A5, 98848, Nouméa Cedex, New Caledonia. [5]Géosciences Environnement Toulouse, CNRS/UPS/IRD/CNES, Université de Toulouse, F-31400, Toulouse, France. [6]Laboratoire Interuniversitaire des Systèmes Atmosphériques (LISA), IPSL, Université Paris Est Créteil (UPEC), Université Paris Diderot (UPD), Créteil, France. [7]IRD/LOPS, IFREMER, CNRS, IUEM, University of Brest, Brest, France. Correspondence and requests for materials should be addressed to C.G. (email: gueu@obs-vlfr.fr)

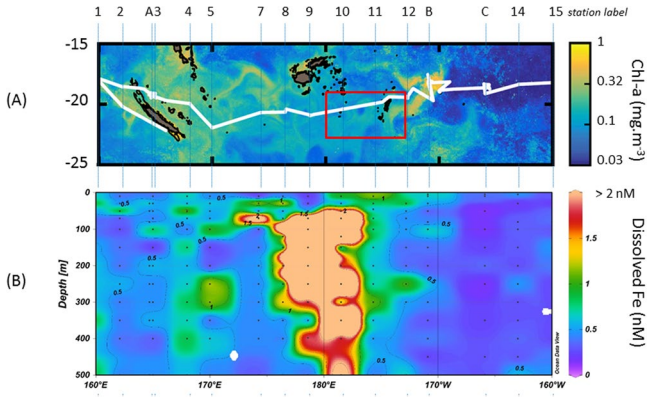


Figure 1. Surface Chlorophyll-a concentration (mg m^{-3}) during the 45-day transect of the OUTPACE cruise (**A**) (The ocean color satellite products are produced by CLS. Figure courtesy of A. De Verneil). (**B**) Cross-section of dissolved Fe nM (0–500 m) (full data set in Supplementary Table 2). The box in 1 A shows the area of the ARGO float journey mapped in Fig. 2A.

average DFe was as high as 3.8 nM, contrasting radically with the <0.3 nM DFe in the adjacent ultra-oligotrophic South Pacific Gyre. Our results reveal that hydrothermal submarine inputs would explain these high DFe concentrations, rather than atmospheric deposition.

Results

Atmospheric source of iron. Atmospheric sources of DFe were suspected to be located west of 170°E longitude, associated with the permanently active Vanuatu volcanoes, and near the Tonga archipelago (175°W longitude). In particular, the Hunga Tonga-Hunga Ha'apai volcano within the Tonga-Kermadec arc erupted between December 19, 2014 and January 24, 2015, before our cruise (February-March 2015). This intense eruption led to the formation of an island whereby volcanic material was emitted into the atmosphere[14]. Total Fe concentrations in our aerosols (Methods and Supplementary Table 1) ranged between 0.013 and 1.96 nmol Fe m^{-3}. Atmospheric Fe being associated with ash or dust, Fe fluxes were estimated using a deposition velocity of 1.4 cm. s^{-1} that is typical of coarse particles[15]. These total Fe fluxes were low (15 to 2361 nmol Fe m^{-2} d^{-1}) and of the same order of magnitude as the mean Fe fluxes in the non-volcanic remote areas of the South Indian Ocean[16]. Indeed, aerosols collected few weeks after the end of the eruption were likely not impacted by emitted particles that certainly moved quickly out of the region, as previously observed for an eruption of the same volcano in 2009[17]. Derived DFe atmospheric inputs to the water column (Supplementary Table 1) ranged from 0.0007 to 0.04 nmol DFe m^{-3}, leading to DFe atmospheric fluxes ranging from 0.85 to 48.7 nmol DFe m^{-2} d^{-1} (0.017 to 0.99 mg DFe m^{-2} yr^{-1}). These DFe fluxes, documented in the WTSP for the first time, are at the lower end of values reported for the remote ocean[18] and support model estimates for dissolved Fe deposition to the WTSP (0.16 to 0.315 mg DFe m^{-2} yr^{-1}[18]). Considering a maximum DFe atmospheric flux of 50 nmol m^{-2} d^{-1} depositing for 40 days (duration of the eruption) and impacting a 20-meter-thick surface mixed layer, the DFe concentration in seawater would have been increased by 0.1 nM. As a result, atmospheric inputs could not explain the DFe concentrations (average up to 3.8 nM) measured in the water column west of Tonga in March 2015.

During the Dec. 2014–Jan. 2015 eruption, satellite images have shown release of volcanic particles directly in the ocean by the newly formed island. This process enhanced not only surrounding ocean turbidity in surface waters very close to the newly formed island, as evidenced by satellite images[14], but also likely the DFe concentrations observed in surface waters (0.80 nM in 0–30 m) around Tonga (Fig. 1B, St 10–11–12). Nevertheless, below the bottom of the mixed layer, the high enrichment in DFe observed all the way down to 500 m (Fig. 1B) could not be explained by that eruption that likely affected mostly locally surface concentrations. As a result, other sources have been explored.

Hydrothermal source of Fe. High DFe concentrations (up to 66 nM) were measured at five profiles at almost all depths between St 7 and St 11, extending zonally over 10 degrees (174 E–175 W longitude) (Fig. 1A). High DFe concentrations (up to 2300 nM) were previously detected in the water column of a shallow volcanic center (~35 km^2 at depth above 1600 m; Monowai volcanic center at the northern end of the Kermadec arc[19]), that were attributed to three major hydrothermal fluid effluents linked to the caldera and cone[19]. Micromolar DFe concentrations were also found at similar depths during submarine eruptions in the Extensional NE Lau Basin[20]. These previous studies argue that shallow arc volcano chains, including the Tonga arc of this study located north of the Kermadec arc, may lead to substantial submarine DFe enrichments. A multibeam bathymetric survey along the 650 km-long Tonga arc report the occurrence of 27 submarine volcanoes[21], nine of them exhibiting volcanic calderas and cones, such as Volcano 1 and 8 (Fig. 2A), which are the closest to our study area. These volcanoes are associated with typical *in situ* hydrothermally-related chemical anomalies in the overlying water column, namely, elevated Fe concentrations[21–25]. Hence, we suspect that the active Volcanos 1 and/or 8 can explain the high DFe concentrations we observed during our cruise (Fig. 1B).

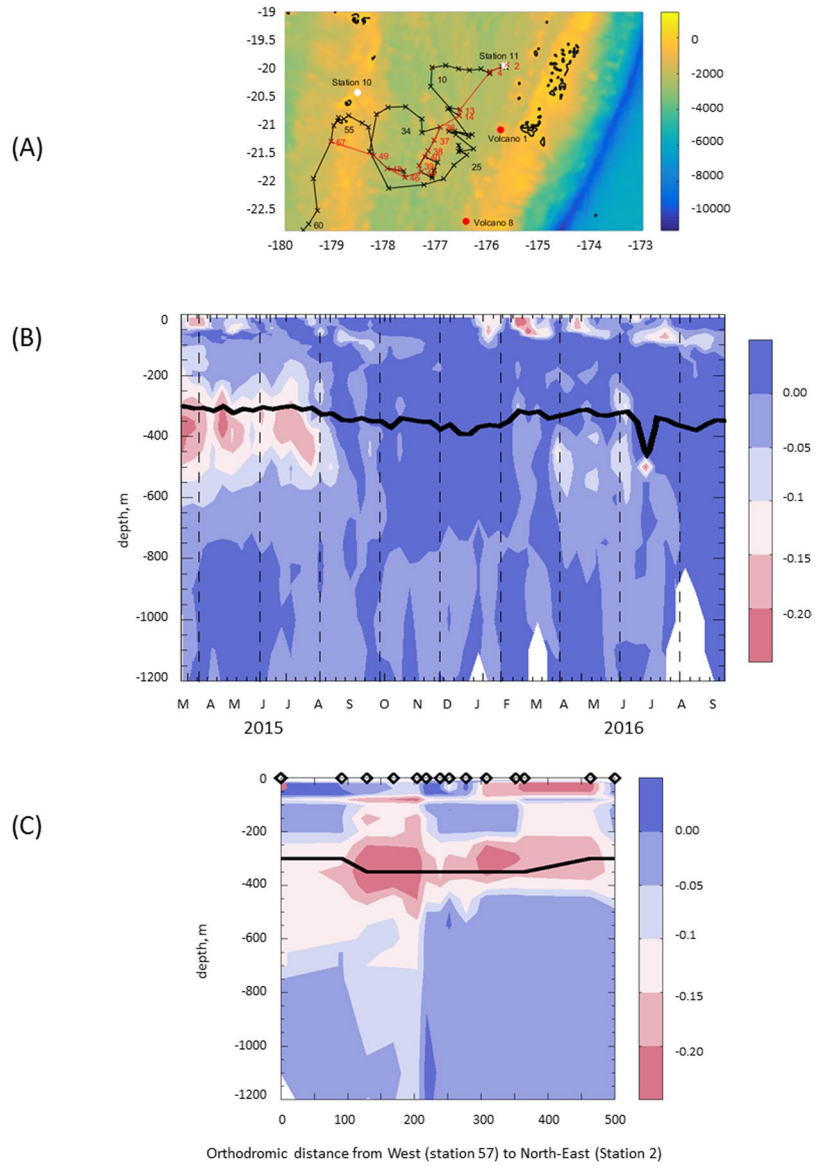


Figure 2. (**A**) Journey of the Argo Float (WMO Id #6901663) (in black) starting at profile 1 performed on March 13, 2015. A non-looping transect (red line between specific stations) is considered in (**C**) to get a spatial mapping, in the float area, away and along the volcanoes. Matlab, 8.6.0.267246 (R2015b), URL link: https://fr.mathworks.com/products/matlab.html was used to generate this map. (**B**) Argo Salinity anomalies along the Argo float journey (anomalies were calculated by subtracting for each profile, a mean annual profile calculated from April 2015 to March 2016), the isopycne 26.0 kg/m^3 is represented by the black line. (**C**) Impact of a low salinity (5 PSU) source located at Volcano 8 (22°50′S, 176°25′W) on salinity: ocean simulation covering January 2014 to May 2015 with a 300 °C source emitting continuously for 2 months (January 2015 and February 2015) (see Methods) on the red section as in (**A**). The graph represents the salinity differences between the simulation with the source and without. Diamonds on the X-axis in (**C**) represent the position of the ARGO profiles along that section; the x-axis being the orthodromic distance in kilometers (0 = profile 57 to 500 = profile 2).

Direct observations of these volcanoes through prior Remotely Operated Vehicle dives revealed the explosive and pulsating nature of the volcanic activity in the WTSP, as evidenced by explosion craters, scoria cones and ash blanket on the caldera floor at ~500 m[23–25]. In this geodynamic setting, hydrothermal activity displays two different but distinct contributions issued from water-rock interaction, most commonly known as "black smokers" and magmatic-gases due to volcanic activity[26]. The magmatic-hydrothermal system such as the one identified at the Hinepuia volcanic center (Kermadec arc, 26°23′S and 177°16′W), discharges gas-rich (liquid elemental sulfur and probable CO_2 gas bubbles) but extremely low salinity fluid (~5 Practical Salinity Unit, PSU) due to subcritical boiling and phase separation[26]. Meanwhile, water-rock hydrothermal systems commonly found at mid-ocean ridges may experience brief (a few days) explosive volcanic events, leading to megaplume formation and dispersion within the water column, i.e., the Juan de Fuca Ridge (North Pacific)[27–29]. In both cases, any submarine volcanic explosion will provoke emission and dispersion of volcanic material (i.e. particles, gases, fluids), which

Source location	volcano 1	21°09′S 175°45′W	source depth, m 450
	volcano 8	22°50′S 176°25′W	source depth, m 500
Source Flux, L.s-1	500–100001.s^{-1}		
Source temp, °C	230–300		
Source Salinity, PSU	5–15–20		
Emission duration, months	2 months, 6 months		

Table 1. Parameters chosen for the submarine emissions in the simulations based on source flux[38,63,64], source temperature[65], and source salinity[66].

will immediately disrupt the chemical and physical signature of the overlying water column. Thus, it appears that "hydrothermalism" can vary in emission fluxes, duration of the venting (age of the plumes) and chemical characteristics. Whether of magmatic or water-rock hydrothermal origin, the "hydrothermalism" corresponds to a submarine input, a terminology that we have chosen to use for our study.

Observed salinity anomalies as a proxy for passive tracer of submarine input. Conservative hydrothermal tracers, such as ^{3}He, were not measured during the OUTPACE campaign, nor manganese, which is also highly enriched in hydrothermal fluids compared to ambient deep ocean concentrations[30]. Over the last 20 years, deep-sea hydrothermal exploration in the world's oceans has been facilitated by the use of Autonomous Underwater Vehicles (AUV) equipped with Conductivity Temperature Depth (CTD) instruments coupled to *in situ* optical devices to detect salinity, temperature, optical back-scatter or Eh anomalies associated with hydrothermal plumes[31]. Similarly, autonomous platforms such as Argo floats have been used by physicists to characterize water masses. We took advantage of the *in situ* hydrological characteristics of the water column recorded by an Argo float deployed during the cruise just after Station 11 in March 2015, to test whether the measured high DFe may be related to hydrothermal activity based on the evidence that magmatic-hydrothermal system discharges low salinity fluids[26]. The float remained in the area for more than eighteen months (Fig. 2A) since its deployment and provided vertical profiles of temperature and salinity every 10 days (a total of 57 profiles). Low salinity anomalies were observed (Fig. 2B), associated with temperature anomalies compensating these fresh salinity anomalies and still resulting in a stable water mass. The dynamics of the heat exchanges of the plume is probably complex at this distance from the source and, as salinity is slightly more conservative, it constitutes a better passive tracer than temperature and was thus chosen in our study.

At depths of 200–500 m (i.e., within the main thermocline), negative salinity anomalies up to −0.2 were observed. The surrounding waters represent a mixture of Pacific Equatorial Water flowing from the east and Western South Pacific Central Water flowing from the south. These water masses located in the lower part of the main thermocline (typical range in sigma between 25 and 26.8 kg. m^{-3}) are characterized by temperature lower than 14 °C and salinity above 35.1[32]. The observed values represent strong anomalies compared to ambient waters' values, even including their variability on seasonal to inter-annual timescales. However, due to meso- and submesoscales and potential entrainment conditions within the water column, it remains difficult to isolate, in such anomalies, the exact contribution resulting from hydrothermal activity. These anomalies are located right in the sector where the high DFe concentrations were measured (Fig. 1). Despite the lack of temporal synopticity with the Fe data collected during the cruise, the Argo data displayed recurrent S anomalies for several months in the area where it stayed since its deployment. Mesoscale activity such as eddies can transport water masses with different characteristics throughout the WTSP[33]. Nonetheless, in the specific depth range of this area, no other typical water masses have S values as low as the ones measured opportunely by this float. A low S water mass may be linked to magmatic and/or water-rock hydrothermal activity, as deep-sea hydrothermal fluids collected immediately after a volcanic eruption at mid-ocean ridge axis[34] or at magmatic-hydrothermal system such as the one at Hinepuia[26], which exhibited unusual extremely low salinity (below 50 mM of chlorine concentration, i.e. salinity <5). This is due to enhanced degrees of phase separation and high H_2, H_2S and CO_2 magmatic degassing[30,35]. Interestingly, Fe solubility during water-rock interactions is significantly increased in low-salinity vapor-dominated hydrothermal fluids[34], implying enhanced DFe flux to the water column.

Modeled salinity anomalies. The possibility that a continuous or intermittent submarine source located at Volcano 1 or Volcano 8 (Fig. 2A) can indeed impact the surface ocean hydrological characteristics is considered by means of an ocean general circulation model (OGCM[36]). The strategy chosen here is not to detail mechanisms of hydrothermal fluid injection into the ocean, which require a thorough knowledge of the source characteristics[37]. In the absence of such data, our strategy was to explore the sensitivity of the model response to submarine emissions in several simulations (Method, Table 1) based on documented durations, flux, salinity and temperature of the emitted fluid over the time-scale defined by the Argo float deployment, (i.e. a few months). Using a relatively idealized 1-D framework, Speer and Rona (1989) explored the adjustment of a high temperature hydrothermal plume in the Pacific venting at 2200 m. They showed that the high temperature hydrothermal fluid (350 °C) achieved neutral buoyancy in the water column at ~200 m above seafloor indicating that, in their case, the maximum vertical course of the fluid emitted at 350 °C was ~200 m. Our 3-D OGCM experiments with state-of-the art 3-D mechanisms at play in the open ocean uses a similar source temperature emission with a very low salinity at an injection depth much shallower (between 450 and 500 mbsl). This permits scientists to explore the fate of the fluid anomalies in the vertical and horizontal directions as realistically as possible. The mean state of our reference model simulation (Methods) compares favorably with the observations in terms of salinity

(Supplementary Fig. 2) and temperature (not shown). Simulations taking into account a flux of 500 l s^{-1}[38] of a 230 °C fluid whose salinity is 20 PSU over a 6-month duration, showed a maximal salinity anomaly ~0.15 weaker than the one observed,with a shorter-duration (2 months) emission. Indeed increasing 20 times the flux (similar to that calculated during a megaplume event[28]), but on a shorter duration, the plume anomaly and intensity increased, and there was good agreement with the observations. When the temperature was increased to 300 °C and the salinity decreased to 5 PSU (Fig. 2C and Supplementary Fig. 3), the model outputs were closer to the observations with the same flux (10 000 l s^{-1}) and duration (2 months). An intermittent event of high magnitude is thus likely to have caused the observed anomaly. The numerous earthquakes recorded in this area during our study period (Supplementary Fig. 5) also support this hypothesis.

Spatial extent of the plume. A low salinity source emitting at 300 °C for two months, led to a first order negative salinity anomaly of ~0.2 at approximately 200 km away from the volcanic source (Supplementary Fig. 3), which is consistent with our observations (Fig. 2B). Remarkably, the modeled submarine source at the caldera seafloor is mixed by convection to a density level consistent with the observations. Modeled salinity anomalies are concentrated within the 200–400 m layer and are also visible in the photic layer (0–90 m). They have a tendency to reach a maximum at approximately 300 m in the meridional section and over several degrees of longitude (Supplementary Fig. 3), at locations in agreement with those observed. Interestingly, the depth reached by these maximum anomalies (~300 m) is 150 m above the depth of the venting, a vertical distance of plume rise compatible with that found more theoretically in previous research[39]. In our case, the model allows to us to follow the anomalies spatially (Supplementary Fig. 3a–d) as the ocean currents advect and diffuse the initial anomalies of Volcano 8. The model also shows how eddies strongly modulate the west/north westward general movement of the initial anomaly. Water mass movements and entrainment of deep waters in upper layers can occur over steep or highly variable topography. Nonetheless, here, this effect has been ruled out since the model exhibits salinity anomalies only when strong and intermittent emissions of a low salinity fluid at Volcano 1 or 8 are considered. The presence of significant salinity anomalies is also detected in Argo atlas from the ISAS13 product[40] with similar properties at depth (and along the same isopycnal surfaces) and the same timing between 2014 and 2015 (Supplementary Fig. 4). The submarine plume diffuses and gets advected. Within a few months, the modeled salinity anomaly propagates over a large area west and north-west of the source (Supplementary Fig. 3), consistent with the main predominant westward currents associated with the subtropical gyre, and modulated by mesoscale activity.

Discussion

Results strongly support the remote and crucial role of a shallow, intermittent and strong submarine source located in the Tonga arc, in shaping the spatial and temporal DFe field observed during OUTPACE (Fig. 1B). Interestingly, the submarine Fe source directly impacted the DFe concentrations in the photic layer. These concentrations reached 3.8 nM on average between stations Stations 7 and 11. Although it was recently hypothesized[41] that Fe from hydrothermal inputs from shallow submarine island arc calderas systems (such as the Tonga–Kermadec arc) could reach the productive zone of the sea surface, this is rarely observed in the ocean as most mid-ocean hydrothermal Fe sources are usually located deeper (~3000 m, e.g.[42]).

As depicted by the spatial propagation of the salinity anomaly (Supplementary Fig. 3), high mesoscale activity in the region such as eddies[33] can transport, disperse and maintain high DFe at the WTSP scale. This statement implies that most of DFe from shallow hydrothermal submarine source is not lost from solution during transport, and mixes almost conservatively with ambient waters. While there is recent evidence for such behavior for DFe from hydrothermal venting in deep-ocean ridges on long spatial scales[42,43], this is the first time that this is assumed for shallow hydrothermal inputs. The maintaining of DFe in solution depends on stabilization mechanisms such as the complexation by organic ligands. Hydrothermal sources release high quantities of organic compounds, enabling the stabilization and preservation of metals such as Fe as organic-binding complexes in the water column[44,45]. Although we only measured total DFe, previous modeling experiments have shown that such ligands are needed to explain the persistence of DFe far from the source emissions in the deep ocean[42]. Whether similar ligands and/or ligands in the surface ocean seawater can explain the persistence of DFe in shallow environment is unknown.

Farther east of Tonga, in the large South Pacific Gyre (SPG), the seafloor goes down to 5000 m, preventing any Fe fertilization of the productive layer from below. Indeed, the ferricline is likely deeper than the pycnocline (found above 400 m[46]) as the concentrations are low and homogeneous throughout the entire 0- to 500-m profile (Fig. 1). Within the gyre at the same latitude, Fitzsimmons and coauthors (2016)[47] calculated vertical diffusive DFe fluxes through the ferricline of 1.5 to 2.8 µmol DFe.m^{-2} yr^{-1} and showed that these fluxes were three orders of magnitude lower than horizontal diffusive fluxes. In the SPG (170–90 W), atmospheric deposition of Fe is among the lowest in the world's oceans[48]. DFe concentrations are in the range of 0.1–0.3 nM in the water column[49,50] (and this study). This likely prevents N_2 fixation from occurring, as rates were close to detection limits in this region during the OUTPACE cruise[51], consistent with former studies[52]. The quasi-absence of N_2 fixation likely explains why dissolved inorganic phosphorus (DIP) is not consumed, accumulates in surface waters in the absence of nitrate, and why the system turns to ultra-oligotrophic conditions[53]. In contrast, west of 170 W, the WTSP waters represent a high DFe, high SST (>28 °C during austral summer conditions) ecosystem receiving DIP-enriched waters flowing from the east through the South Equatorial Current (SEC). N_2 fixation rates measured during OUTPACE in this region are among the highest reported in the global ocean (average 631 ± 286 µmol N m^{-2} d^{-1}[51] compared to the common range of 10–100 µmol N m^{-2} d^{-1} reported for the global tropical ocean[54]. Our study reveals that a shallow submarine Fe source in the region of the Tonga arc fertilizes photic waters of the WTSP. This is of the utmost importance as it has potentially strong impacts on ecosystem functioning as N_2 fixation fuels nearly all new primary production and organic matter export in the WTSP during austral summer

conditions[55]. Indeed, between this shallow submarine Fe source and the DIP-enriched waters of the SEC, conditions in the WTSP are likely ideal for diazotrophs to bloom extensively and probably explains the hotspot of N_2 fixation[1].

Future investigations are required to quantify this Fe flux from below, study the scavenging/mixing fate of hydrothermal plumes in the water column at the local and regional scales, characterize submarine sources (hydrothermal vs. volcanic), characterize metal vs. ligand sources, and quantify the biogeochemical impact of shallow submarine hydrothermal sources on biological pump processes such as primary production, nitrogen fixation, and export production.

Methods

DFe measurements. A total of 186 water samples from 16 vertical profiles (0–500 m) were sampled using a Titanium Rosette mounted with 24 Teflon-coated 12 L GoFlos and operated along a Kevlar cable. GoFlos were transported inside a clean container, and samples were filtered directly from the GoFlos through 0.2-µm cartridges (Sartorius Sartrobran-P-capsule with a 0.45-µm prefilter and a 0.2-µm final filter), following trace metal clean protocols described previously[50]. DFe concentrations were measured by flow injection with online preconcentration and chemiluminescence detection using the exact protocol, instrument, and analytical parameters as described previously[50]. Some of the samples were analyzed at sea, and the remaining acidified samples were analyzed at LOV. The reliability of the method was monitored by analyzing the D1 SAFe seawater standard[56], and an internal acidified seawater standard was measured every day in order to monitor the stability of the analysis. The same methodology was also used to analyze DFe from dissolution experiments. Analyses of SAFe D1 standard[56] for DFe averaged 0.62 ± 0.06 nmol/kg ($n = 9$), which agrees well with the consensus value of 0.67 ± 0.04 nmol/kg as of May 2013 (http://www.geotraces.org/science/intercalibration/322-standards-and-reference-materials). Considering the wide range of [DFe], calibration curves and pre-concentration times were adapted in order to measure DFe concentrations within the calibration curves. Preconcentration was 120 s for most of the samples and down to 10 s for the highest [DFe]. All the measured concentrations are reported in Supplementary Table 2.

Aerosol sampling and measurements. Ten aerosol samples were collected during the cruise transect (Supplementary Fig. 1) for total Fe concentrations measurements and to quantify their potential DFe release in seawater. Aerosol samples were collected using a sampling device designed to avoid ship contamination. This sampling device (fully described in[48]) was installed at the look-out post in the front on the ship (10 m above sea level). Briefly, the device was able to collect four samples simultaneously at ~20 L. min^{-1}, (onto polycarbonate, 47-mm diameter, 0.45-µm porosity previously acid-cleaned with a 2% solution of HCl (Merck, Ultrapur, Germany) and thoroughly rinsed with ultra-pure water and dried under a laminar flow bench and stored in acid-cleaned Petri dishes). The total amount of air pumped through each filter was recorded using volumetric counters. Wind direction and speed were measured continuously close to the sampling device using a wind vane coupled to an anemometer. Depending on the wind conditions, the device operated either in 'sampling' mode or 'protection' mode. Sampling mode (air pumped through the filters) was activated only if wind was oriented at an open 90-degree angle upwind at a speed higher than 2 m s^{-1}. Protection mode (no air pumped, device closure, and filters protected) was activated if wind conditions could generate sample contamination. A total of 10×4 samples (Aero1 to Aero11) were collected and used for (1) total iron analysis (SFX) and (2) dissolution experiments.

Aerosols total iron concentrations. The total iron concentrations were obtained by wavelength dispersive X-ray fluorescence (WD-XRF) for samples collected during the cruise, using a PW-2404 spectrometer by PANalytical following exactly the same protocol as described by[57].

Aerosols dissolution experiments. Dissolution experiments were conducted on aerosol samples. Using acid-cleaned Sartorius filtration units (volume 0.250 L) and seawater collected at 4 different stations along the transect, the samples were subjected to two contact times with filtered seawater: the first contact was at one minute, and the second contact was at 24 hours. DFe was measured in the filtrates by FIA (see above).

Argo Float data. Information on the Arvor float trajectory and data can be found at: http://www.coriolis.eu.org/Data-Products/Data-Delivery/Argo-floats-by-WMO-number, entering its float number: 6901663. Salinity are reported with a resolution on the order of 0.01 pss-78 (practical salinity scale, according to the 1978 practical salinity scale).

Simulation of salinity anomaly. The OUTPACE and float data, despite being quite informative, were not meant for a study oriented towards submarine sources. Hence, we decided that the best strategy was to rely on the results from an OGCM simulation. We thus used the Regional Oceanic Modeling System (ROMS[58] to explore the impact of volcanic sources at the ocean floor on salinity and to compare our simulations with the numerous *in situ* observations allowed by the Argo Float (see previous section). As well as this reference simulation, we performed several simulations with submarine sources located either at Volcano 1 or Volcano 8 and characterized by different physico-chemical parameters (Table 1). These sources are modeled as rivers discharging from the caldera seafloor. Our 3-D model framework was chosen over a 1-D diffusive model[39] because our model not only includes the vertical diffusion processes of[39] but also permits to follow the fate of the water masses 3-dimensionally as obviously observed off the hydrothermal source (Supplementary Fig. 3).

Our regional configuration is based on that of[36]. The model domain is [165°E–167.5°W/23.5°S–15°S], and the spatial resolution is 1/12° in latitude and longitude. It has 41 terrain-following vertical levels, leading to a vertical resolution of 2 to 5 -m within 50 m of the ocean surface and 10 to 20 -m in the thermocline. Open boundary conditions[59] are specified using the mercator ocean reanalysis (http://marine.copernicus.eu/services-portfolio/access-to-products/?option=com_csw&view=details&product_id=GLOBAL_ANALYSIS_FORECAST_

PHY_001_024). The reference simulation spans January 2014 to May 2015, and the model initial state is taken from that reanalysis. The model time step is 1/3 hours. At six-hour intervals, heat, fresh and momentum fluxes used to force the reference model simulation were calculated using[60] bulk formulae with NCEP2[61] surface atmospheric inputs for the heat and freshwater fluxes, but the ERA interim[62] was used for the wind stress to maintain compatibility with the ocean re-analysis at the boundaries.

References

1. Bonnet S., Caffin, M., Berthelot H. & Moutin T. A hot spot of N_2 fixation in the western tropical South Pacific pleads for a spatial decoupling between N_2 fixation and denitrification. *Proc Natl Acad Sci USA*, https://doi.org/10.1073/pnas.1619514114 (2017).
2. Falkowski, P. G., Barber, R. T. & Smetacek, V. Biogeochemical controls and feedbacks on ocean primary production. *Science* **281**, 200–206 (1998).
3. Moore C.M. *et al*. Processes and patterns of oceanic nutrient limitation, *Nature Geoscience*, https://doi.org/10.1038/ngeo1765 (2013).
4. Rueter, J. G., Hutchins, D. A., Smith, R. W. & Unsworth, N. L. Iron nutrition of Trichodesmium in *Marine pelagic cyanobacteria: Trichodesmium and other Diazotrophs* 289–306 (Springer, 1992).
5. Berman-Frank, I., Cullen, J. T., Shaked, Y., Sherrell, R. M. & Falkowski, P. G. Iron availability, cellular iron quotas, and nitrogen fixation in Trichodesmium. *Limnol Oceanogr.* **46**, 1249–1260 (2001).
6. Shiozaki, T., Kodama, T. & Furuya, K. Large-scale impact of the island mass effect through nitrogen fixation in the western South Pacific Ocean. *Geophys Res Lett.* **41**, 2907–2913 (2014).
7. Lin I. *et al*. Fertilization potential of volcanic dust in the low-nutrient low-chlorophyll western North Pacific subtropical gyre: Satellite evidence and laboratory study. *Global Biogeochem Cy*. **25** (2011).
8. Achterberg, E. P. *et al*. Natural iron fertilization by the Eyjafjallajökull volcanic eruption. *Geophys Res Lett.* **40**, 921–926 (2013).
9. Tagliabue, A., Aumont, O. & Bopp, L. The impact of different external sources of iron on the global carbon cycle. *Geophys Res Lett.* **41**, 920–926 (2014).
10. Pelletier, B., Calmant, S. & Pillet, R. Current tectonics of the Tonga–New Hebrides region. *Earth Planet Sc Lett.* **164**, 263–276 (1998).
11. German, C. R. *et al*. Hydrothermal impacts on trace element and isotope ocean biogeochemistry. *Phil. Trans. R. Soc. A* **374**, 20160035 (2016).
12. Schlitzer, R. Quantifying He fluxes from the mantle using multi-tracer data assimilation. *Phil. Trans. R. Soc. A* **374**, 20150288 (2017).
13. Campbell, L., Carpenter, E. J., Montoya, J. P., Kustka, A. B. & Capone, D. G. Picoplankton community structure within and outside a Trichodesmium bloom in the southwestern Pacific Ocean. *Vie et milieu* **55**, 185–195 (2005).
14. Global Volcanism Program, Report on Hunga Tonga-Hunga Ha'apai (Tonga), Weekly Volcanic Activity Report, 21 January–27 January 2015, Sennert, S K (ed.) (Smithsonian Institution and US Geological Survey, 2015).
15. Dulac, F., Buat-Ménard, P., Ezat, U., Melki, S. & Bergametti, G. Atmospheric input of trace metals to the western Mediterranean: uncertainties in modelling dry deposition from cascade impactor data. *Tellus B* **41**, 362–378 (1989).
16. Heimburger, A., Losno, R. & Triquet, S. Solubility of iron and other trace elements in rainwater collected on the Kerguelen Islands (South Indian Ocean). *Biogeosciences* **10**, 6617–6628 (2013).
17. Shi, W. & Wang, M. Satellite observations of environmental changes from the Tonga volcano eruption in the southern tropical Pacific. *Int J Remote Sens* **32**, 5785–5796 (2011).
18. Mahowald, N. M. *et al*. Atmospheric iron deposition: global distribution, variability, and human perturbations. *Annu Rev Mar Sci.* **1**, 245–278 (2009).
19. Leybourne, M. I. *et al*. Submarine magmatic-hydrothermal systems at the Monowai volcanic center, Kermadec arc. *Economic Geology* **107**, 1669–1694 (2012).
20. Resing, J. A. *et al*. Active submarine eruption of boninite in the northeastern Lau Basin. *Nat Geosci.* **4**, 799–806 (2011).
21. Stoffers P. & Worthington T. Shipboard Scientific Party, Cruise Report SONNE 167, Louisville Ridge: Dynamics and magmatism of a mantle plume and its influence on the Tonga- Kermadec subduction system: Reports of the Institut für Geowissenschaften, Universität Kiel, no. 20, 276 p. (2003)
22. Massoth, G. J. *et al*. *Intra-oceanic subduction systems: Tectonic and magmatic processes* 119–139 (Geological Society of London, 2003)
23. Massoth, G. *et al*. Multiple hydrothermal sources along the south Tonga arc and Valu Fa Ridge. *Geochem, Geophy, Geosy*. **8** (2007).
24. Stoffers, P. *et al*. Submarine volcanoes and high-temperature hydrothermal venting on the Tonga arc, southwest Pacific. *Geology* **34**, 453–456 (2006).
25. Hekinian, R., Mühe, R., Worthington, T. J. & Stoffers, P. Geology of a submarine volcanic caldera in the Tonga Arc: Dive results. *J Volcanol Geoth Res* **176**, 571–582 (2008).
26. Stucker, V. K., Walker, S. L., de Ronde, C. E., Caratori Tontini, F. & Tsuchida, S. Hydrothermal Venting at Hinepuia Submarine Volcano, Kermadec Arc: Understanding Magmatic-Hydrothermal Fluid Chemistry. *Geochem, Geophy, Geosy.* **18**, 3646–3661 (2017).
27. Gendron, J. F., Cowen, J. P., Feely, R. A. & Baker, E. T. Age estimate for the 1987 megaplume on the southern Juan de Fuca Ridge using excess radon and manganese partitioning. *Deep-Sea Res.* **40**, 1559–1567 (1993).
28. Baker, E. T., Massoth, G. J. & Feely, R. A. Cataclysmic hydrothermal venting on the Juan de Fuca Ridge. *Nature* **329**, 149–151 (1987).
29. Baker, E. T. *et al*. Hydrothermal event plumes from the CoAxial seafloor eruption site, Juan de Fuca Ridge. *Geophy Res Lett.* **22**, 147–150 (1995).
30. Von Damm, K. L. Seafloor hydrothermal activity: black smoker chemistry and chimneys. *Ann Rev Earth Pl Sc.* **18**, 173–204 (1990).
31. German, C. R. *et al*. Hydrothermal exploration with the autonomous benthic explorer. *Deep-Sea Res.* **55**, 203–219 (2008).
32. Gasparin, F., Maes, C., Sudre, J., Garcon, V. & Ganachaud, A. Water mass analysis of the Coral Sea through an Optimum Multiparameter method. *J Geophys Res-Oceans* **119**, 7229–7244 (2014).
33. Rousselet, L., Doglioli, A. M., Maes, C., Blanke, B. & Petrenko, A. A. Impacts of mesoscale activity on the water masses and circulation in the Coral Sea. *J Geophys Res-Oceans* **121**, 7277–7289 (2016).
34. Pester, N. J., Ding, K. & Seyfried, W. E. Jr. Magmatic eruptions and iron volatility in deep-sea hydrothermal fluids. *Geology* **42**, 255–258 (2014).
35. Butterfield, D. A. *et al*. Seafloor eruptions and evolution of hydrothermal fluid chemistry. *Philos T Roy Soc A* **355**, 369–386 (1997).
36. Menkes, C. E. *et al*. About the role of Westerly Wind Events in the possible development of an El Nino in 2014. *Geophys Res Lett* **41**, 6476–6483 (2014).
37. Lavelle, J. W., Wetzler, M. A., Baker, E. T. & Embley, R. W. Prospecting for hydrothermal vents using moored current and temperature data: Axial Volcano on the Juan de Fuca Ridge, northeast Pacific. *J Phys Ocean* **31**, 827–838 (2001).
38. Thurnherr, A. M. & Richards, K. J. Hydrography and high-temperature heat flux of the Rainbow hydrothermal site (36 14′ N, Mid-Atlantic Ridge). *J Geophys Res-Oceans* **106**, 9411–9426 (2001).
39. Speer, K. G. & Rona, P. A. A model of an Atlantic and Pacific hydrothermal plume. *J Geophys Res-Oceans* **94**, 6213–6220 (1989).
40. Gaillard, F., Reynaud, T., Thierry, V., Kolodziejczyk, N. & von Schuckmann, K. *In-situ* based reanalysis of the global ocean temperature and salinity with ISAS: Variability of the heat content and steric height. *J. Clim.* **29**, 1305–1323 (2016).
41. Hawkes, J. A., Connelly, D. P., Rijkenberg, M. J. & Achterberg, E. P. The importance of shallow hydrothermal island arc systems in ocean biogeochemistry. *Geophys Res Lett.* **41**, 942–947 (2014).

42. Resing, J. A. *et al*. Basin-scale transport of hydrothermal dissolved metals across the South Pacific Ocean. *Nature* **523**, 200–203 (2015).
43. Fitzsimmons, J. N. *et al*. Iron persistence in a distal hydrothermal plume supported by dissolved-particulate exchange. *Nat Geosci.* **10**, 195–201 (2017).
44. Sander, S. G. & Koschinsky, A. Metal flux from hydrothermal vents increased by organic complexation. *Nat Geosci.* **4**, 145–150 (2011).
45. Kleint C., Hawkes J.A., Sander S.G & Koschinsky A., Voltametric investigation of hydrothermal iron speciation. *Frontiers in Marine Science* **3**, https://doi.org/10.3389/fmars.2016.00075 (2016).
46. Moutin, T., Doglioli, A. M., De Verneil, A. & Bonnet, S. Preface: The Oligotrophy to the UlTra-oligotrophy PACific Experiment (OUTPACE cruise, 18 February to 3 April 2015). *Biogeosciences* **14**, 3207–3220 (2017).
47. Fitzsimmons, J. N. *et al*. Dissolved iron and iron isotopes in the southeastern Pacific Ocean. *Global Biogeochem Cy.* **30**, 1372–1395 (2016).
48. Wagener T., Guieu C., Losno R., Bonnet S. & Mahowald N. Revisiting atmospheric dust export to the Southern Hemisphere ocean: Biogeochemical implications. *Global Biogeochem Cy*. **22**, https://doi.org/10.1029/2007GB002984 (2008).
49. Fitzsimmons J. N., Boyle E. A. & Jenkins W. J. Distal transport of dissolved hydrothermal iron in the deep South Pacific Ocean. *Proc Natl Acad Sci USA*, **111** (2014).
50. Blain, S., Bonnet, S. & Guieu, C. Dissolved iron distribution in the tropical and sub tropical South Eastern Pacific. *Biogeosciences* **5**, 269–280 (2008).
51. Bonnet, S. *et al*. In depth characterization of diazotroph activity across the Western Tropical South Pacific hot spot of N_2 fixation, *Biogeosciences* In proof (2018).
52. Raimbault, P. & Garcia, N. Evidence for efficient regenerated production and dinitrogen fixation in nitrogen-3 deficient waters of the South Pacific Ocean: impact on new and export production estimates. *Biogeosciences* **5**, 323–338 (2008).
53. Moutin, T. *et al*. Phosphate availability and the ultimate control of new nitrogen input by nitrogen fixation in the tropical Pacific Ocean. *Biogeosciences* **5**, 95–109 (2008).
54. Luo, Y. W. *et al*. Database of Diazotrophs in Global Ocean: Abundance, Biomass, and Nitrogen Fixation Rates. *Earth System Science Data* **4**, 47–73 (2012).
55. Knapp, A. N. *et al*. Distribution and rates of nitrogen fixation in the western tropical South Pacific Ocean constrained by nitrogen isotope budgets. *Biogeosciences* In proof (2018).
56. Johnson, K. S. *et al*. Developing standards for dissolved iron in seawater. *Eos, Transactions American Geophysical Union* **88**, 131–132 (2007).
57. Desboeufs, K. *et al*. Chemistry of rain events in West Africa: evidence of dust and biogenic influence in convective systems. *Atmos. Chem. Phys.* **10**, 9283–9293 (2010).
58. Shchepetkin, A. F. & McWilliams, J. C. The regional oceanic modeling system (ROMS): a split-explicit, free-surface, topography-following-coordinate oceanic model. *Ocean Modelling* **9**, 347–404 (2005).
59. Marchesiello, P., McWilliams, J. C. & Shchepetkin, A. Open boundary conditions for long-term integration of regional oceanic models. *Ocean Modelling* **3**, 1–20 (2001).
60. Fairall, C. W. F., Bradley, E. F., Rogers, D. P., Edson, J. B. & Young, G. S. Bulk parameterization of air-sea fluxes for Tropical Ocean-Global Atmosphere Coupled-Ocean Atmosphere Response Experiment. *J. Geophys. Res. Oceans* **101**, 3747–3764, https://doi.org/10.1029/95JC03205 (1996).
61. Kanamitsu, M. *et al*. NCEP-DOE AMIP-II reanalysis (R-2). *Bull. Amer. Meteor. Soc.* **83**, 1631–1643 (2002).
62. Dee, D. P. *et al*. The ERA-Interim reanalysis: Configuration and performance of the data assimilation system. *Q. J. Roy. Meteorol. Soc.* **137**, 553–597 (2001).
63. Baker, E. T., Massoth, G. J. & Feely, R. A. Cataclysmic hydrothermal venting on the Juan de Fuca Ridge. *Nature* **329**, 149–151 (1987).
64. German, C. R. *et al*. Heat, volume and chemical fluxes from submarine venting: A synthesis of results from the Rainbow hydrothermal field, 36 N MAR. *Deep-Sea Res.* **57**, 518–527 (2010).
65. Rizzo, A. L. *et al*. Kolumbo submarine volcano (Greece): An active window into the Aegean subduction system. *Scientific reports* **6**, 28013 (2016).
66. Pester, N. J., Ding, K. & Seyfried, W. E. Jr. Magmatic eruptions and iron volatility in deep-sea hydrothermal fluids. *Geology* **42**, 255–258, https://doi.org/10.1130/G35079.1 (2014).

Acknowledgements

This research is a contribution of the OUTPACE (Oligotrophy from Ultra-oligoTrophy PACific Experiment) project (https://outpace.mio.univ-amu.fr/), funded by the Agence Nationale de la Recherche (grant ANR-14-CE01-0007-01), the LEFE-CyBER program (CNRS-INSU), the Institut de Recherche pour le Développement (IRD), the GOPS program (IRD) and the CNES (BC T23, ZBC 4500048836). The OUTPACE cruise (http://dx.doi.org/10.17600/15000900) was managed by the MIO (OSU Institut Pytheas, AMU) from Marseille (France). The authors thank the crew of the R/V L' Atalante for outstanding shipboard operations. We acknowledge the help of Justine Louis in collecting the seawater samples on board. The Argo data were collected and made freely available by the International Argo Program and the national programs that contribute to it (http://www.argo.ucsd.edu, http://argo.jcommops.org). The Argo Program is part of the Global Ocean Observing System. We are grateful to Gilles Rougier and Lucio Bellomo for the Argo floats deployment during the cruise. G. Rougier and M. Picheral are warmly thanked for their efficient help in CTD rosette management and data processing, as well as C. Schmechtig for the LEFE-CyBER database management. All data and metadata are available at the following web address: http://www.obs-vlfr.fr/proof/php/outpace/outpace.php. J. Resing and two anonymous reviewers are warmly thanked for their help in improving this manuscript.

Author Contributions

C.G., S.B. and T.M. designed research. C.G. analyzed D.Fe., K.D. analyzed aerosols, A.P. and C.Ma. analyzed and interpreted Argo data (including Fig. 2 and supp Fig. 4), V.C. contributed to Fig. 2, wrote the discussion on hydrothermal anomaly and proposed conditions for anomaly modeling (Table 1), C. Me. carried out the modeling (including Fig. 2C, supp Fig. 2, supp Fig. 3). All authors contributed to the preparation of the manuscript and the discussion of the results.

Additional Information

Supplementary information accompanies this paper at https://doi.org/10.1038/s41598-018-27407-z.

Competing Interests: The authors declare no competing interests.

Publisher's note: Springer Nature remains neutral with regard to jurisdictional claims in published maps and institutional affiliations.

Open Access This article is licensed under a Creative Commons Attribution 4.0 International License, which permits use, sharing, adaptation, distribution and reproduction in any medium or format, as long as you give appropriate credit to the original author(s) and the source, provide a link to the Creative Commons license, and indicate if changes were made. The images or other third party material in this article are included in the article's Creative Commons license, unless indicated otherwise in a credit line to the material. If material is not included in the article's Creative Commons license and your intended use is not permitted by statutory regulation or exceeds the permitted use, you will need to obtain permission directly from the copyright holder. To view a copy of this license, visit http://creativecommons.org/licenses/by/4.0/.

© The Author(s) 2018